Numerical simulations of wake characteristics of a horizontal axis tidal stream turbine using Actuator Line Model

Mohammad H. Baba-Ahmadi*

School of Science and Engineering, University of Dundee, Dundee, DD1 4HN, UK

Ping Dong

School of Engineering, The Quadrangle, The University of Liverpool, Brownlow Hill, Liverpool, L69 3GH, UK

Abstract

The wake of a laboratory scale tidal stream turbine in a shallow water channel with a turbulent inflow is simulated using the hybrid LES/ALM technique, which combines large eddy simulation with the actuator line method. The turbulent inlet conditions are generated using the mapping method to avoid a precursor running and large space for saving data. The numerical results demonstrated the usefulness of the mapping technique as well as some shortcomings that still remain to be addressed. Good agreement between numerical predictions and experimental data is achieved for both the mean and turbulent characteristics of the flow behind the turbine. The examination of changes in turbulence intensity and turbulent kinetic energy in the streamwise direction confirms the existence of a peak and transition to a highly turbulent flow about three diameters downstream of the turbine, which means that the distinct characteristics of the streamwise changes of turbulence intensity or turbulent kinetic energy may serve as an effective indicator for the flow regime transition and wake behaviour.

Keywords: Tidal stream turbine, Actuator line method, Large eddy simulation, Turbulent inflow generation

1. INTRODUCTION

The interest in tidal stream energy worldwide is driven by three aspects of the resource: it is renewable, predictable (different from wave and wind), and amply available. At the present time, the marine energy industry is lagging behind the wind energy industry. Many scientific and technological hurdles still need to be overcome before the identified potential of marine energy can be fulfilled. Accurate simulation of flow through the tidal stream turbines (TSTs) using computational fluid dynamics (CFD) plays a key role to better understand TST flow structure, design efficient TST blades and accurately predict their performance especially in tidal arrays.

*Corresponding author

Email addresses: m.babaahmadi@dundee.ac.uk (Mohammad H. Baba-Ahmadi), ping.dong@liverpool.ac.uk (Ping Dong)

Simulating the flow behind a tidal stream turbine poses several challenges, especially in the near-wake region where the blades trailing vorticity is concentrated in tip and root vortices, subject to rapid deformation and turbulent diffusion. Study of the near-wake is important both for rotor and far-wake analysis and is therefore of concern to both TST and TST arrays design. Among the available techniques, Actuator Disc Method (ADM), Blade Element Momentum (BEM) and 3D blade-resolved methods are commonly used in the simulation of TSTs. ADM and BEM techniques allow for fast simulations but are unable to accurately simulate flow features such as unsteady wake development. The 3D blade-resolved simulations, on the other hand, are able to account for unsteady effects but, as the blade boundary layers must be discretised, would require a large computational resource to provide resolution in the vicinity of the blades. Over the past decade, Actuator Line Methods (ALM), first developed for wind turbines by Sørensen & Shen [1] and later reformulated by Mikkelsen [2] into a primitive (pressure-velocity) variable model, have also been used to study flows through horizontal axis turbines. These models simulate the 3D flow field but represent the turbine blades using body forces distributed along rotating lines, thus bridging the gap between the time-resolved accuracy of the 3D blade-resolved models and the speed of ADM and BEM models. In most TST applications, ALM is integrated in a Reynolds-Averaged Navier-Stokes (RANS) solver. There is not much published work addressing the application of Large Eddy Simulation (LES) coupled with the ALM technique for simulating tidal turbines. A notable work is that of Churchfield *et al.*[3] who used the LES/ALM technique to simulate TST arrays. The authors, in their previous work [4], also used this technique for simulating a laboratory scale tidal turbine to validate the method by comparison with detailed measurements.

The treatment of inlet conditions for LES is important to ensure accurate prediction of the flow field as, in many cases, the fluid behaviour within the domain is determined in large part by the inlet behaviour. However, formulation of inlet conditions is not straightforward because the inlet flow must include stochastically-varying components with proper temporal and spatial correlations. The most accurate way of achieving this is to run a precursor calculation to generate a library of turbulence, either prior to the simulation of the actual flow system or concurrently with it, and then to transfer the data from the library simulation to the main domain inlet. Churchfield *et al.*[3] ran a horizontally-periodic precursor simulation to create turbulent flow data which are then used as the inflow into a tidal turbine array two rows deep and infinitely wide.

There exist other techniques to generate inflow conditions known as synthetic methods, in which some form of random fluctuations are generated and combined with the mean flow at the inlet. In their study, Gant and Stallard [5] attempted to provide unsteady turbulent inflow generated by imposing fluctuations onto a power-law mean velocity profile. The fluctuations were derived from either a von Kármán spectral approach or a synthetic eddy method. Gant and Stallard found that the unsteady flow imposed at the upstream boundary decays with downstream distance, as is to be expected with RANS models. Nevertheless, they found that wake recovery with downstream distance was much enhanced by the use of unsteady inflow. Troldborg *et al.* [6] used a synthetic method to generate turbulent inflow conditions and applied the method to investigate the influence of different inflow conditions on wind turbine wake properties [7]. In their study,

the turbulent fluctuations are produced in a cross section upstream of the rotor through the use of body forces. The introduced turbulence field was generated in advance using the Mann algorithm [8]. The output of this algorithm is a spatial box of equidistantly spaced turbulence, which is transformed into a time series through Taylors frozen turbulence hypothesis. The generated turbulence is then introduced into a non-sheared inflow. Their simulations using different techniques to model the turbine showed that the differences in mean wake velocity and turbulent kinetic energy observed in laminar inflow were significantly reduced using turbulent inflow even for very low turbulence intensities. This result highlights the point that proper inflow modelling and characterization is important in accurately simulating TST arrays. The authors used a synthetic method to generate inlet conditions in their previous work [4] for simulating a laboratory scale TST using the LES/ALM technique. In their study, due to lack of the experimental mean velocity profiles, the inlet velocity conditions were generated using the 1/7 power law velocity profile superimposed with white noise of a prescribed intensity.

In this study, the LES/ALM technique is used to simulate a laboratory-scale TST. The CFD results are compared to experimental data generated at the University of Hull [9]. The purpose of the paper is to demonstrate the capability and accuracy of the LES/ALM method in simulating TSTs and reproduce the peak of the turbulent kinetic energy corresponding to the flow regime transition behind the turbine already predicted numerically by the authors in [4]. For specifying the turbulent inlet conditions, the mapping method developed by the authors based on the recycling techniques is used [10, 11]. This method effectively avoids the long time and large space required in the precursor calculation techniques and generates inflow conditions with more reliable time and space correlations in comparison to the synthetic methods.

2. NUMERICAL MODELLING

2.1. Large eddy simulation

The governing equations for LES method are obtained by filtering the time-dependent Navier-Stokes equations in physical space, such that those eddies which are below a certain size are filtered out. The resulting equations thus only govern the dynamics of the large scales, while the smaller scales usually are modelled by some eddy-viscosity-based sub-grid scale (SGS) models. The filtered incompressible Navier-Stokes equations in velocity-pressure variables are written as

$$\frac{\partial \bar{u}_i}{\partial x_i} = 0 \tag{1}$$

$$\frac{\partial \bar{u}_i}{\partial t} + \frac{\partial (\bar{u}_i \bar{u}_j)}{\partial x_j} = -\frac{1}{\rho}\frac{\partial \bar{p}}{\partial x_i} + \nu \frac{\partial^2 \bar{u}_i}{\partial x_j^2} + \frac{\partial \tau_{ij}}{\partial x_j} + f_{i,\epsilon} \tag{2}$$

where the bar denotes filtering, and $\bar{u}_j = u_j - u_j^{sgs}$ is the resolved-scale velocity vector, which is the instantaneous velocity vector, u_j, minus the SGS velocity vector, u_j^{sgs} and $f_{i,\epsilon}$ is the body force provided by the actuator line method described later in section 2.2. The turbulent stresses are modelled with an eddy

viscosity as

$$\tau_{ij} = -\nu_t \left(\frac{\partial \bar{u}_i}{\partial x_j} + \frac{\partial \bar{u}_j}{\partial x_i} \right) + \frac{2}{3} k \delta_{ij} \tag{3}$$

The eddy viscosity is determined by solving an extra equation for the sub-grid turbulent kinetic energy as

$$\frac{\partial k}{\partial t} + \bar{u}_j \frac{\partial k}{\partial x_j} = \frac{\partial}{\partial x_j} \left(\frac{\nu_t}{\sigma_k} \frac{\partial k}{\partial x_j} \right) - \tau_{ij} \frac{\partial \bar{u}_i}{\partial x_j} - \epsilon_k, \tag{4}$$

where

$$\epsilon_k = C_\epsilon \frac{k^{3/2}}{\Delta} \qquad , \qquad \nu_t = C_k k^{1/2} \Delta \tag{5}$$

and σ_k, C_k and C_ϵ are model coefficients introduced in [12] and Δ is the local cell size.

2.2. Actuator line method

In LES, turbulence is largely generated in the wall boundary layer by resolving it on a fine mesh. This would require very small cell sizes and time steps, and makes LES very expensive for simulating high Reynolds number flows. To overcome this problem, in this study the geometry of the turbine is not resolved and instead, the turbine is represented using a method developed by Sørensen & Shen [1]. Using this method, resolving the boundary layer in detail is avoided and the loading on the rotor blades is calculated from airfoil data. With ignoring the blade geometry, theoretically turbulence will be generated from the movement of the body forces and the interaction of the moving body forces with the bed boundary layer.

In this technique, a three-dimensional Navier-Stokes solver is coupled with the actuator line method in which body forces are distributed along rotating lines representing the turbine blades. Therefore, full 3D Navier-Stokes simulations predict the flow field and loads on each blade are determined from the local angle of attack and tabulated airfoil data. The computational cost for LES/ALM computations is somewhat comparable to that of unsteady full RANS computations because LES/ALM avoids the procedure of resolving the boundary layer of the blades.

Having the flow field together with the blade geometry, a blade element approach combined with tabulated 2D airfoil characteristics is used to determine the loads on the rotor blades. Figure 1 shows a cross-sectional airfoil element at radius r in the (θ, z) plane. The velocity triangle shown in Figure 1 is used to calculate the local velocity relative to the rotating blade as follows:

$$V_{rel} = \sqrt{\mathrm{v}_z^2 + (\Omega r - \mathrm{v}_\theta)^2} \tag{6}$$

where Ω is the angular velocity and $\mathrm{v_z}$ and v_θ present the axial and tangential velocities, respectively. As shown in Figure 1, the local angle of attack is given by $\alpha = \phi - \gamma$, where γ denotes the local pitch angle and ϕ is the flow angle between $\mathrm{V_{rel}}$ and the rotor plane calculated as:

$$\phi = \tan^{-1} \left(\frac{\mathrm{v}_z}{\Omega r - \mathrm{v}_\theta} \right) \tag{7}$$

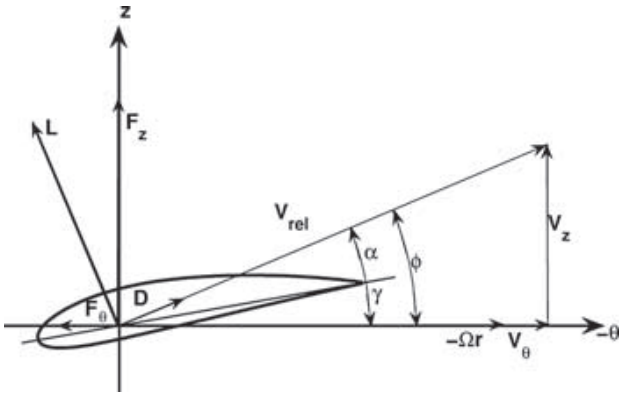

Figure 1: Cross-sectional airfoil element showing velocity and force vectors.

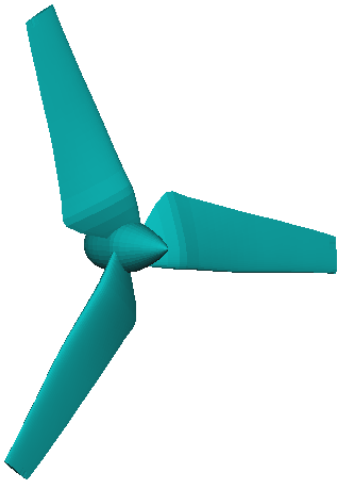

Figure 2: Schematic of the scale HATT.

The force per spanwise unit length normalised by density can be calculated using the determined angle of attack and relative velocity as:

$$\mathbf{f}_{2D} = \frac{1}{2} c V_{rel}^2 (C_L \mathbf{e}_L + C_D \mathbf{e}_D) \tag{8}$$

here $\mathrm{C_L} = \mathrm{C_L}(\alpha, \mathrm{Re})$ and $\mathrm{C_D} = \mathrm{C_D}(\alpha, \mathrm{Re})$ present the lift and drag coefficients, respectively, c denotes the chord length, Re is the chord-based Reynolds number, and $\mathbf{e}_L$ and $\mathbf{e}_D$ are the unit vectors in the lift and the drag directions, respectively.

To avoid singular behaviour and numerical instability, the modelled blade forces are distributed smoothly on several mesh points along and away from the actuator lines using a 3D Gaussian projection. In practice, the resulting body force, $\mathbf{f}_\epsilon$, is then formed by taking the convolution of the computed force, $\mathbf{f}_{2D}$ and a regularization kernel η_ϵ as shown below:

$$\mathbf{f}_\epsilon(\mathbf{x}) = \sum_{i=1}^{B} \int_0^R F_1 \mathbf{f}_{2D}(r) \eta_\epsilon(|\mathbf{x} - r\mathbf{e}_i|) dr \tag{9}$$

where B is the number of blades, $\mathbf{e}_i$ is the unit vector of the $\imath$th blade direction, $|\mathbf{x} - r\mathbf{e}_i|$ is the distance between cell-centred grid points and points at the $\imath$th actuator line and η_ϵ is the regularization kernel defined as

$$\eta_\epsilon(r) = \frac{1}{\epsilon^3 \pi^{3/2}} \exp\left[-r^2/\epsilon^2\right] \tag{10}$$

here ϵ is a parameter that serves to adjust the concentration of the regularized load and takes a value between 2 and 3 cell sizes, Troldborg [13]. $\mathrm{F_1}$ appeared in Eq. 9 is a tip correction that accounts for the 3D rotational effects developed by Shen *et al.* [14] and is applied to the calculated 2D forces in this study. The function $\mathrm{F_1}$ is defined as

$$F_1 = \frac{2}{\pi} \cos^{-1}\left[\exp\left(-g\frac{B(R-r)}{2r\sin\phi}\right)\right] \tag{11}$$

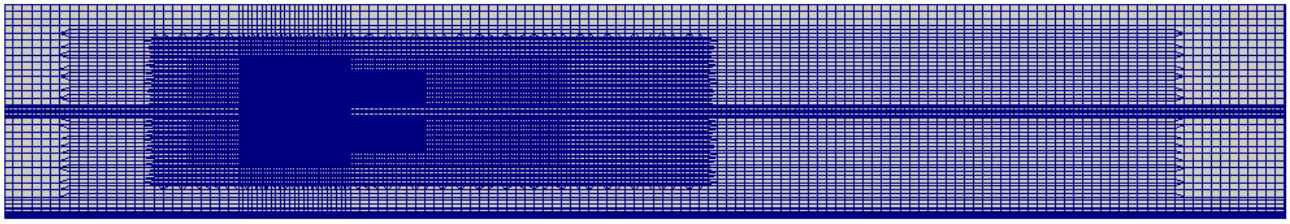

Figure 3: Side view of the computational domain.

where B is the number of blades, R is the rotor radius, ϕ denotes the flow angle and g is a function defined as

$$g = \exp(-0.125(B\Omega R/U - 21)) + 0.1 \tag{12}$$

where U is the bulk velocity at the inlet.

2.3. Flow solver

The filtered incompressible Navier-Stokes equations together with the SGS model are solved using the CFD code library OpenFOAM [15, 16]. The governing equations are discretised using the finite volume method. Although the solver is unstructured, the grid used here is composed of hexahedral elements and could be described in a structured way. Integration of the dependent variables over each cell, together with application of Gauss' theorem, generates a set of discretised equations with the divergence terms represented as fluxes across the cell faces, evaluated using an appropriate centred second order interpolation scheme (gamma scheme). Time integration is carried out by the Crank-Nicholson scheme, which is second order in time. Following the procedure of Rhie & Chow [17] a Poisson equation is constructed which implements the incompressibility condition (Eq. 1), and the equation set solved sequentially using the PISO algorithm. Solution is performed implicitly by matrix inversion using Incomplete Cholesky Conjugate Gradient methods.

2.4. Computational domain

In this study, a horizontal axis laboratory scale TST comprising of three blades has been numerically simulated with the hybrid LES/ALM technique. All geometrical and model details conform to the experimental set up of Jordan *et al.* [9]. The experiment was performed in the Total Environment Simulator (TES) at the University of Hull. The test channel was constructed with a width of 1.6m and a length of 11m. The flow depth used during the experiment was 0.6m with the turbine located at a depth of 0.3m to ensure the rotor was far from the water surface. Figure 2 shows schematically the 0.2 m diameter, three-bladed configuration of the horizontal axis tidal turbine (HATT) used in the experiment. The rotor was run at a rotational speed $\Omega = 162.3$ rpm and an inflow bulk velocity U = 0.33 m/s.

Unsteady computations were carried out using a Cartesian mesh of 2.8×10^6 mesh points in a domain of size 5.5m $\times$ 1.0m $\times$ 0.6m with the finest cell size nearly R/30 in the turbine plane, where R is the rotor

radius. Figure 3 shows a vertical slice of the mesh at the rotor plane. From a numerical point of view, a discretization of R/30 has been found sufficient for the LES/ALM simulations, Sørensen & Shen [1] and Shen *et al.* [14]. The rotor centre was located at a section 1.5m downstream of the inlet and a height 0.307m from the bed. The time step is chosen to be 10^{-3}R/U and simulation is carried out for a total of 80.41 s. The time series are averaged for the last 50 s to remove the effect of initial transience and obtain stable time-averaged quantities. The simulation was run for 6200 cpu-hours. In regions near the bed and the short cylinder modelling the nacelle, a wall model developed based on Spalding's law [18] is used to avoid using a very fine mesh and increasing computational costs. The calculated y+ for cells near the bed and the cylinder are chosen to be approximately 4 and 12 respectively.

In the simulation, the side boundaries are set to periodic conditions. Applying the mapping technique, inlet conditions are numerically generated using the mean and root mean square (rms) velocity components experimentally measured for a turbulent flow in a plain channel without the rotor and support. On the downstream boundary, the normal gradient of velocity is zero, and the resulting velocity flux through that boundary is adjusted to maintain global continuity. The gradient of pressure normal to the upstream is zero and pressure is fixed on downstream. The upper boundary is approximated as an impenetrable, no stress lid, instead of simulating a free surface [19]. No slip condition and zero normal gradient for pressure are applied for the bed boundary and short cylinder modelling the nacelle.

2.5. Turbulent inflow conditions

The turbulent inflow conditions are constructed using the mapping technique developed by the authors [10, 11] for large eddy simulation with some modifications. As explained in [10, 11], in this method, the velocity a short distance downstream of the inlet to the main domain is sampled and the flow velocity data are reintroduced back into the domain inlet, creating an inlet section integrated into the main computational domain in which variable artificial body forces and velocity corrections are imposed with feedback control to force the flow toward desired mean and turbulent profiles. In the present simulation, all three mean velocity components, u, v and w and three rms velocity components, u', v' and w' are calculated in the inlet section and fed to the main flow. The main modification to the method is in the time frequency of applying velocity corrections in the inlet section. The recent work on the mapping technique shows that this frequency strictly depends on the mesh resolution near the inlet and the time step of simulation.

For this test case, the mean and rms velocity components measured for a turbulent flow in the plain channel without the rotor and support are applied as the desired mean and turbulent profiles used in the mapping technique to generate the inflow conditions. Figure 4 shows the plots of normalised streamwise mean velocity component and three rms velocity components. The measured data are presented by the black dotted lines and the applied inlet conditions and the mean profiles at 1D upstream of the turbine are shown by the red and blue solid lines respectively. Although the lack of experimental data for the section one diameter upstream to the turbine prevents a fuller evaluation of the simulation, the results that have been examined are considered reasonable, particularly for the calculated mean velocity profile as compared with

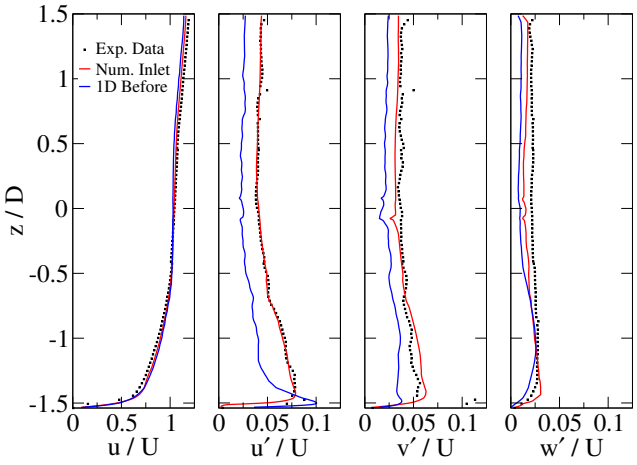

Figure 4: Streamwise mean velocity component and rms velocity components at the inlet.

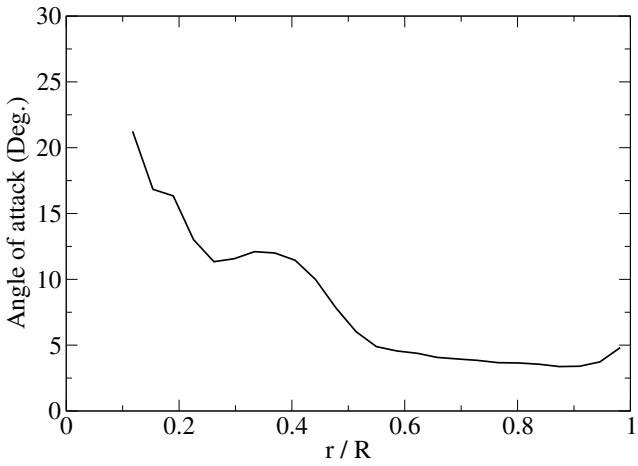

Figure 5: Angle of attack on the actuator lines. .

that at the inlet. The predicted turbulent fluctuations do show some deviations from the experimental data but they are well within the acceptable ranges for this type of TST simulations. The flow at the section 1D before the turbine plane experiences a lower turbulence level in comparison to the inlet section. This is likely to be due to the imperfectness of the mapping method used and work to improve the method is currently under way.

2.6. Airfoil data

Since there was no experimental airfoil data of the lift and drag coefficients, C_L and C_D, available for the simulated rotor, these data for all blade sections at the corresponding Reynolds numbers, were generated numerically using XFOIL. The XFOIL code has been validated against other numerical methods and experimental data at both low and moderate angles of attack. As the numerical results for the angle of attack (AoA) presented in Figure 5 show, for the simulated experiment, there are $|\text{AoA}| \leq 12°$ for the most parts of the blade and regarding a local chord-based Re about 30,000 at 0.75 blade span, the XFOIL outputs should be reliable [20]. For the first three points, the available experimental data for NACA0018 are used with some modifications. To avoid any inconsistency and have a smooth transition for airfoil data between various sections of the blade, 20 sections were generated in the radial direction using Auto CAD.

3. RESULTS AND DISCUSSION

The numerical results for the mean velocity components u, v and w and rms velocity components u′, v′ and w′ are compared to the experimental data in Jordan *et al.* [9]. The experimental data and numerical results are presented with symbols (square) and solid lines respectively throughout this paper unless stated explicitly otherwise. The quantities are normalised by the inflow bulk velocity and the turbine diameter which are U = 0.33 m/s and D = 0.2m respectively. The presented results are for the test case with a clockwise

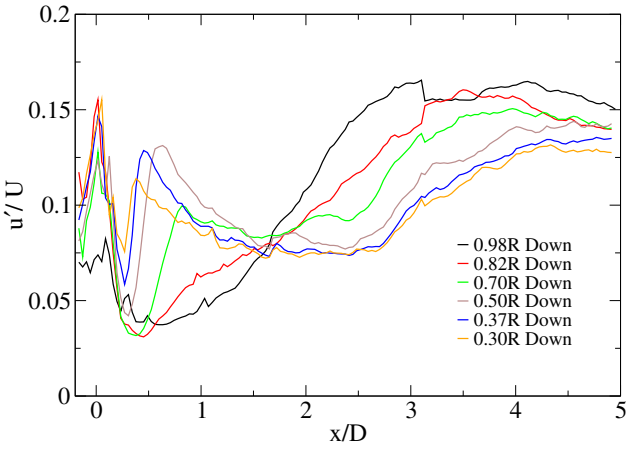

Figure 6: Longitudinal turbulence intensity at various heights below the turbine downstream (Exp.).

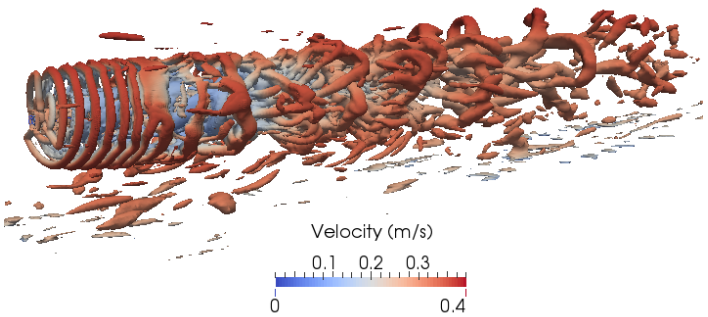

Figure 7: Instantaneous view of the flow field. Isometric view of the second invariant of the velocity gradient tensor coloured by the mean velocity.

rotational speed $\Omega = 162.3$rpm when looking downstream. The experimental data are available for two vertical planes starting from the turbine plane up to 5D downstream of the turbine. The first plane covers the points from the bed to the free surface and includes the rotor axis. The second plane is at the left hand side of the first one when looking downstream with a distance 0.5D from that. The first and second planes are referred to as the mid-section and off-section respectively in this paper.

In the experiment, at the connection plane between the rotor shaft and housing there is a sharp jump in the radius as explained by Jordan *et al.* [9] . This configuration changes the flow direction around the rotor axis effectively and prevents from developing hub vortices started at the rotor plane in the flow. Figure 6 shows a sharp jump in the longitudinal turbulence intensity (u'/U) around 0.3D behind the turbine where is the connection plane explained above. The plots indicate it affects the flow in a zone around the rotor axis radially up to about %75 of the blade radius and longitudinally up to 3D behind the turbine and because of breaking hub vortices, the flow structure completely changes in this zone. Nonetheless, the most advantage of this experiment in comparison to other experiments is covering the points starting from the turbine plane which makes it an excellent choice to investigate the flow structure particularly tip vortices immediately behind the turbine. In the numerical simulation only the nacelle is modelled. It is modelled by a short cylinder with the hub radius. Because of the explained difference between ensembled turbine configurations in the experiment and numerical simulation, the results are not comparable for the zone radially up to %75 of the blade radius and longitudinally up to 4D behind the turbine. Here, the results are compared for the points at distances 1D, 2D, 3D, 4D and 5D far from the turbine plane. Figure 7 gives an instantaneous view of the flow field behind the turbine and clearly shows a flow regime transition further downstream. Figure 7 presents an isometric view of the second invariant of the velocity-gradient tensor sometimes called the 'Q criterion' coloured by the mean velocity.

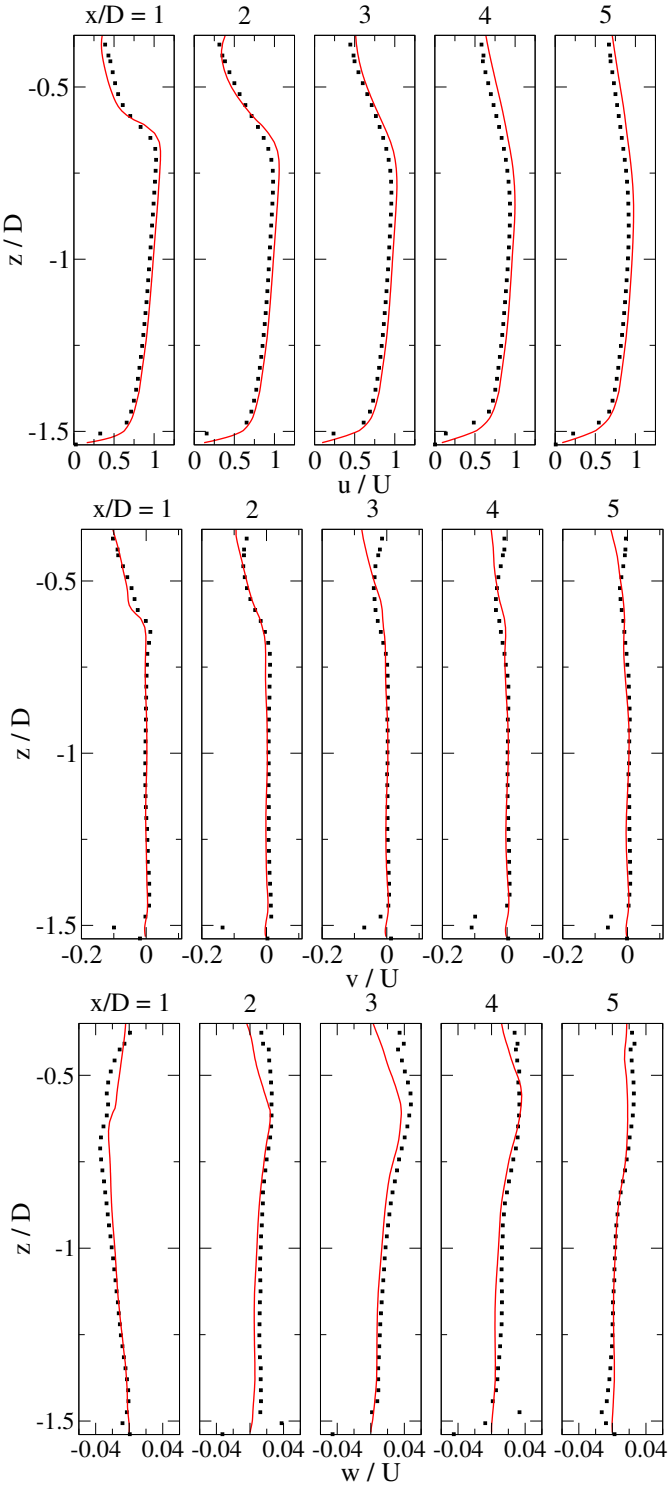

Figure 8: Mean streamwise, transverse and vertical velocity components downstream at the mid-section; squares: Exp., solid lines: CFD.

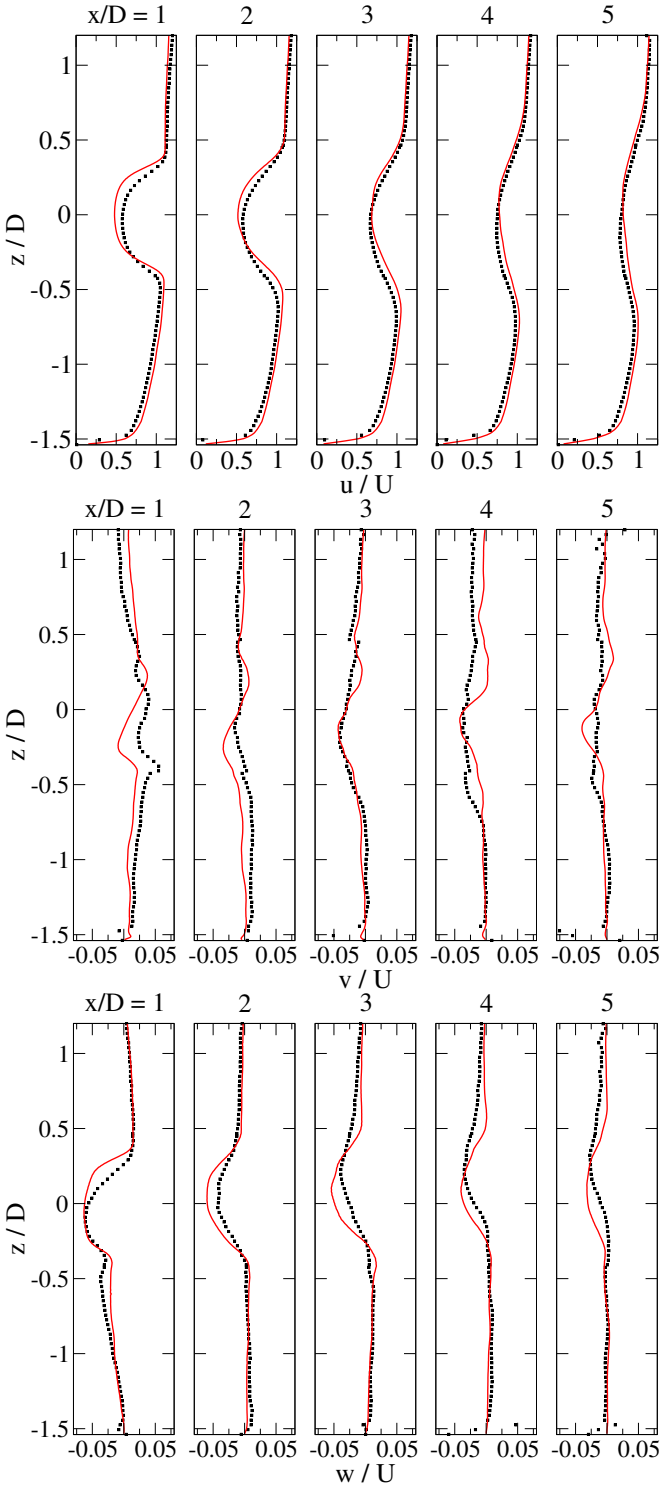

Figure 9: Mean streamwise, transverse and vertical velocity components downstream at the off-section; squares: Exp., solid lines: CFD.

3.1. Mean flow

Figure 8 shows the normalised mean velocity components behind the turbine at the mid-section. The top, middle and bottom frames show the normalised u, v and w respectively. The plots show a very good agreement for the numerical results especially for the streamwise velocity component u. For the other components there are some discrepancies around the tip vortices zone and near the wall. For the first part, it can be said that the transverse and vertical components, v and w are more affected by the changes of flow structure caused by the different ensembled turbine configurations explained above. The discrepancies appeared near the bed can be referred to inaccuracy in the measurements. Because v and w components must go to zero for an impenetrable bed in a channel.

Figure 9 shows the normalised mean velocity components behind the turbine at the off-section. The normalised u, v and w are presented in the top, middle and bottom frames respectively. The comparison shows a reasonable agreement with discrepancies in some parts. Considering the results at distances 1D and 2D behind turbine shows that in comparison to the experimental data, the numerical results are more symmetric around the $z/D = 0$ in the region $|z/D| \leq 0.5$. This is due to absence of the vertical support in the numerical simulation that makes it a symmetric configuration. Here similar to the results shown in Figure 8, the level of inaccuracy for v and w components are higher than that for u component around the $z/D = 0$ and can be explained with the same reason.

3.2. Turbulent flow field

The numerical results for the rms velocity components u', v' and w' at the mid-section are compared with the experimental data in Figure 10. The comparison shows a satisfying agreement between numerical and experimental data for three components with some deviations around the tip vortices zone at distances 1D and 2D behind the turbine. There are two possible reasons to be considered for this inaccuracy. The first reason goes back to the nature of the actuator line method. As explained in the section 2.2, in ALM, the blade is replaced with a line and the blade boundary layer is not resolved. In fact, in ALM, the turbulence generated in the boundary layer and fed to the flow in the real case, is ignored. The blade vibrations in the real case which are absent in the numerical simulation can be considered as a secondary reason. Because of the above reasons the level of turbulence intensity in the numerical simulation should be less than that in the experiment for distances up to 2-3 diameters behind the turbine as shown in Figure 10. Some discrepancies are also seen near the wall for v' and w' which can be referred to inaccuracy in the measurements as explained in section 3.1.

Figure 11 presents the results for the rms velocity components u', v' and w' at the off-section in the top, middle and bottom frames respectively. There are some deviations in the numerical results downstream of the turbine especially at distances 1D and 2D similar to discrepancies appeared in the results shown in Figure 10 and can be demonstrated with similar reasons. There is a new issue in the numerical results for u' which needs to be examined. Comparing the results for u' shown in the top frame indicates a weaker agreement at

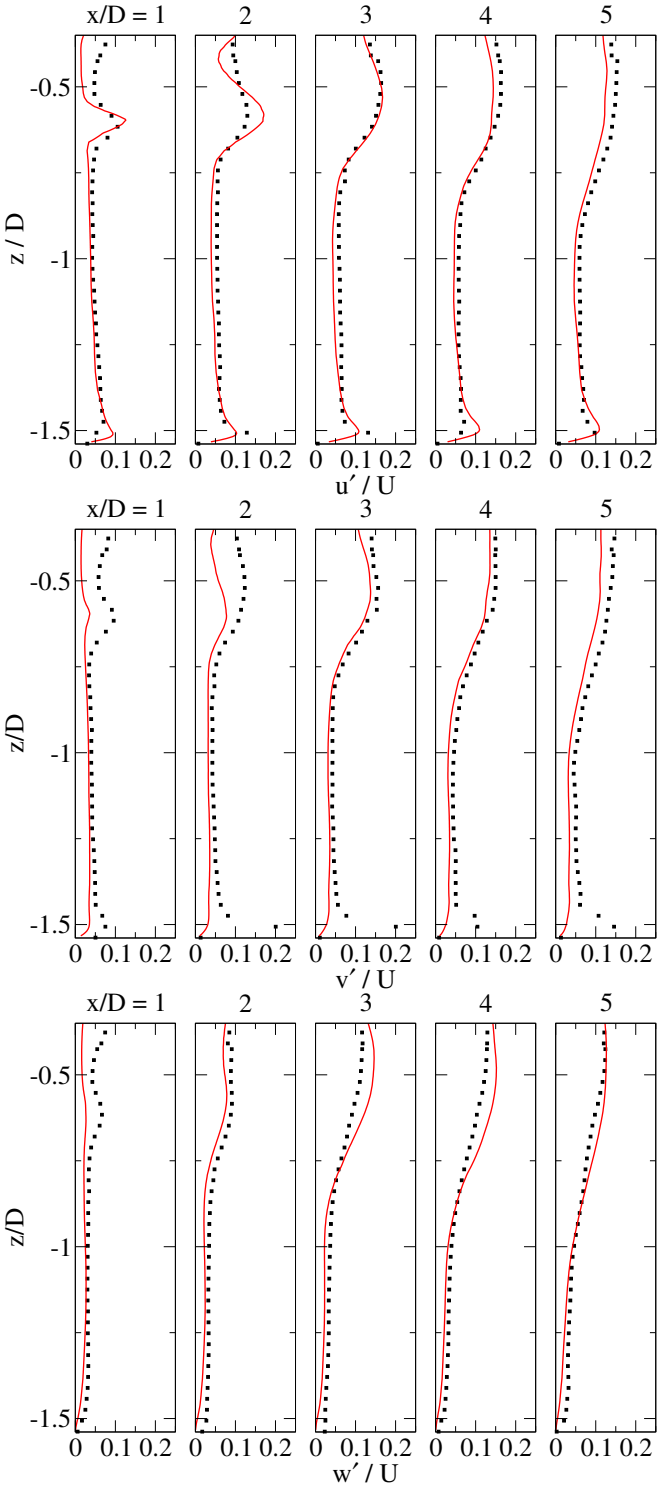

Figure 10: Streamwise, transverse and vertical rms velocity components downstream at the mid-section; squares: Exp., solid lines: CFD.

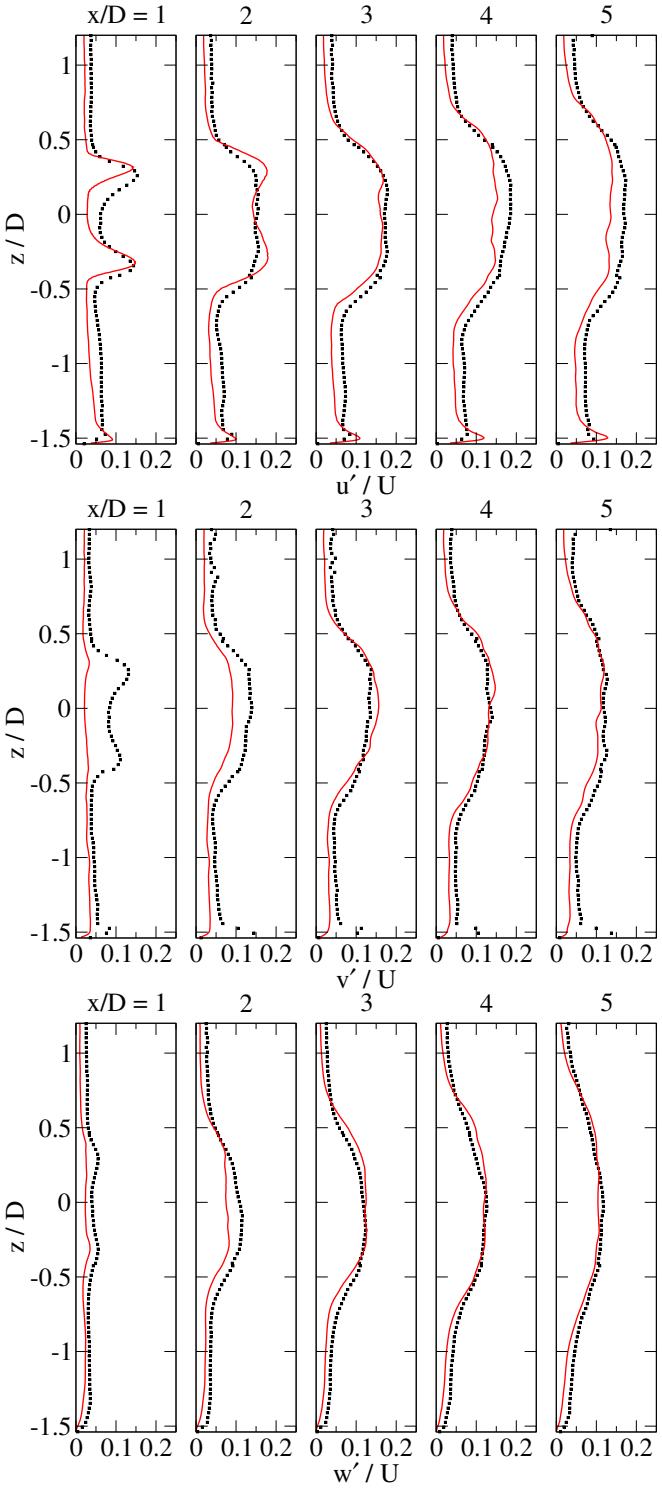

Figure 11: Streamwise, transverse and vertical rms velocity components downstream at the off-section; squares: Exp., solid lines: CFD.

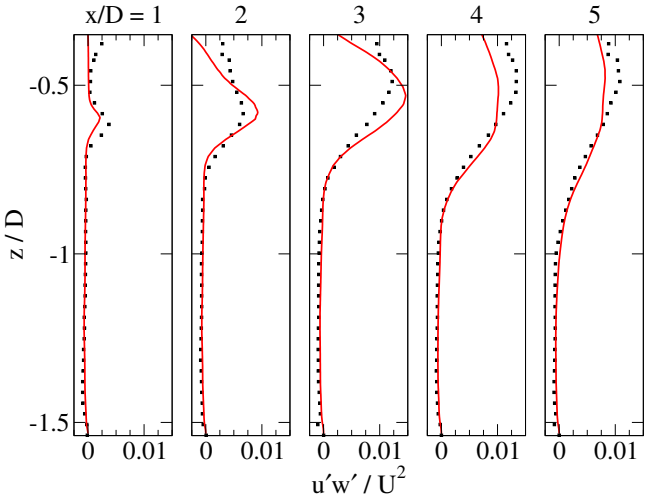

Figure 12: Velocity fluctuations ($u'w'$) downstream at the mid-section; squares: Exp., solid lines: CFD.

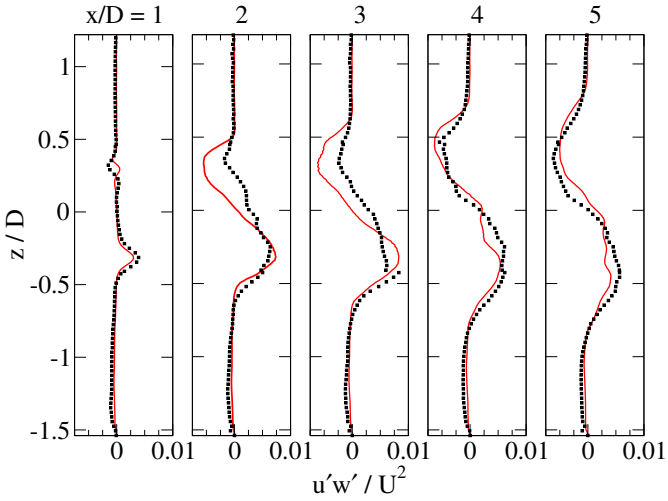

Figure 13: Velocity fluctuations ($u'w'$) downstream at the off-section; squares: Exp., solid lines: CFD.

distances 4D and 5D respect to that at distance 3D behind the turbine which is in contrast to what is seen for the other components in the middle and bottom frames. As a possible reason it can be referred to use an isotropic turbulence model in this simulation while Tedds *et al.* [21] have reported a strongly anisotropic nature for the near-wake turbulence. Well understanding of this situation requires further studies using other turbulence models.

The numerical results for velocity fluctuations $u'w'$ at the mid- and off-section are compared with the experimental data in Figures 12 and 13 respectively. Plots presented in Figure 12 show that although numerical results have some deviations from experimental data around the tip vortices zone but they are still reasonable and trends are well captured. Ignoring the turbulence generated in the blades' boundary layer and the blades' vibrations because of the nature of the ALM technique can be considered as a reason for appeared discrepancies. The absence of vertical support and the use of an isotropic turbulence model in this simulation could be the other possible reasons. Figure 13 presents a comparison between the numerical and experimental data for $u'w'$ at the off-section and it shows good agreement except for results at 2 and 3 diameters downstream particularly at the top half of the channel where numerical results approximately show an antisymmetric behaviour around the rotor axis while the experimental data are less antisymmetric. The main reason for this difference most likely should be ignoring the vertical support in the numerical simulation which provides a symmetric configuration around the rotor axis.

Figures 14 and 15 show a comparison between the numerical and experimental results for the normalised turbulent kinetic energy (TKE) at different distances behind the turbine at the mid-section and off-section respectively. The TKE differs from the sub-grid kinetic energy and is defined as $\mathrm{TKE} = \frac{1}{2}(\mathrm{u'^2} + \mathrm{v'^2} + \mathrm{w'^2})$. Since TKE is not a measured parameter and is calculated using the mentioned relation, the figures show similar issues as those appeared in the measured values, u′, v′ and w′.

A closer look at the results in both mid- and off-sections for the points above the bed up to $z/D = -0.5$

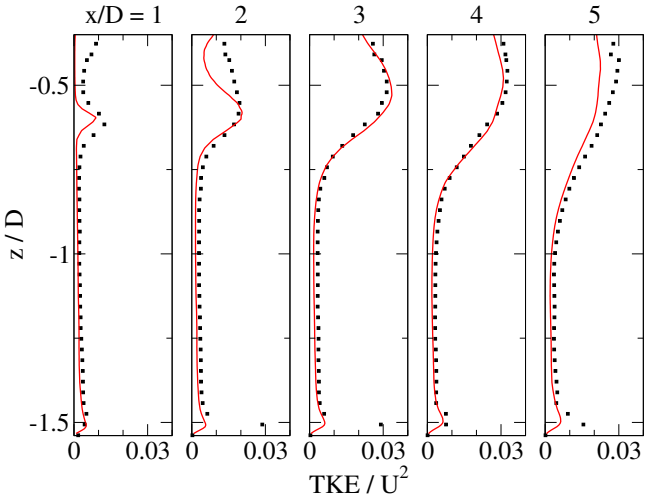

Figure 14: Turbulent kinetic energy behind the turbine at the mid-section; squares: Exp., solid lines: CFD.

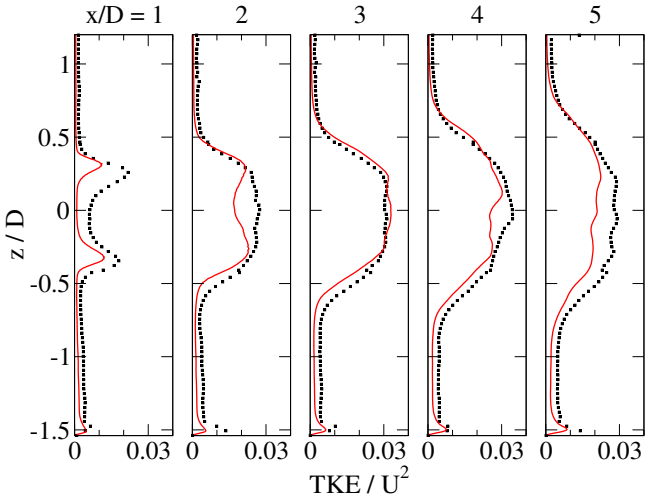

Figure 15: Turbulent kinetic energy behind the turbine at the off-section; squares: Exp., solid lines: CFD.

shows a considerable difference between two sections. While for the mean velocity components, u, v and w, the agreement between the numerical and experimental results shown in Figures 8 and 9 are comparable, for the rms velocity components, u′, v′ and w′, the level of discrepancy for the results in the off-section (Figure 11) is higher than that for the results in the mid-section (Figure 10). This difference can be referred to the dominant turbulence. Since the mid-section is at the middle of a high turbulent flow downstream of the turbine, the dominant turbulence is the turbulence generated by the wakes and the results in this section are no longer affected by the inflow turbulence. But in the off-section, possibly the effect of inflow turbulence would be considerable and an imperfect simulation of the turbulent flow at the inlet generates a higher mismatching in the results in the off-section.

3.3. Wake characteristics

Figure 16 presents the changes of the longitudinal turbulence intensity, u'/U, in the streamwise direction on the mid-section at two radii, 0.82R and 0.98R below the rotor axis. The numerical results show a monotonously decreasing behaviour for u′ further downstream similar to that reported by Tedds *et al.* [21] and Baba-Ahmadi and Dong [4] for the other experiment as shown in Figure 17. Baba-Ahmadi and Dong [4] numerically predicted a second peak in the sreamwise direction in the turbulence intensity and turbulent kinetic energy behind the turbine and showed that the monotonous reduction of the above parameters is started from the second peak rather than from the first peak that appeared at the turbine plane. Unfortunately for the experiment reported by Tedds *et al.* [21] no experimental data was available to confirm this prediction. As depicted in Figure 16, the experimental data here are available for the points immediately behind the turbine and confirm the existence of the second peak in the turbulence intensity and TKE in the flow. Physically, the occurrence of the first peak near the rotor is most likely due to the periodic nature of the flow resulted from the turbine rotation. Just downstream of this, there is a region where the wake

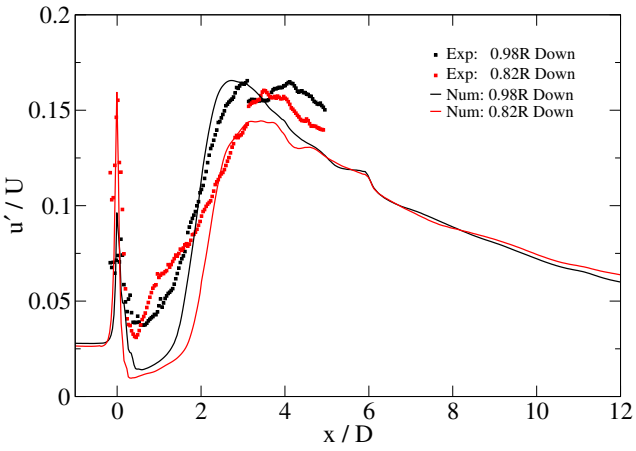

Figure 16: Longitudinal turbulence intensity at two heights below the turbine downstream.

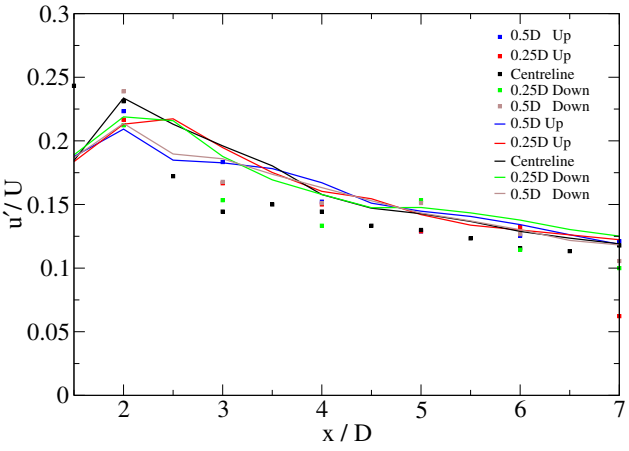

Figure 17: The maximum of longitudinal turbulence intensity at the various heights downstream adapted [4].

is composed of a set of coherent vortices (see Figure 7) and much of the periodic nature of the flow is lost as they mix and diffuse through the flow, corresponding to the low TKE region up to about 1.8D. Further downstream, these vortices break-down into small scale turbulent flow, causing the increase of TKE, thus the second peak. The variation of shear-production arising from the mean-shear between the wake and surrounding flow may also contribute to the second peak but this requires further investigation. Figure 16 also shows a reasonable agreement between numerical and experimental data around two peaks. The comparison shows some deviations between results for the points between two peaks. The possible reasons for this mismatching were explained in section 3.2.

4. CONCLUSION

The LES/ALM technique has been applied to simulate a laboratory scale tidal stream turbine in a shallow water channel with a turbulent inflow and validated using results from an experiment developed at the University of Hull [9]. The simulation uses the mapping method for generating turbulent inlet conditions to model the real inflow of the experiment. In general, satisfying agreements between the computational and experimental results are seen for mean velocity, mean turbulent fluctuations and turbulent kinetic energy. The reasonable agreements seen in comparisons particularly for the turbulent characteristics show the reliability of the applied mapping method to construct turbulent inflows.

An examination on streamwise changes of the longitudinal turbulence intensity, u'/U, immediately downstream of the turbine obtained from the experiment and numerical simulation confirms the existence of the second peak in rms velocity components and TKE in the flow behind the turbine. This situation was already predicted by the authors numerically in their previous work [4] and implies that the decreasing behaviour of turbulence intensity and turbulent kinetic energy further downstream started from the second peak and not from the first peak observed at the turbine plane. Investigating the turbulent characteristics in near-wake is still in progress and results will be presented in detail separately.

The examination of the experimental data shows that the configuration of the nacelle can influence the flow structure in the near-wake strongly. Since the laboratory-scale TST experiments are usually referred for evaluating the numerical simulations, the above situation may suggest to use a downwind configuration for the experiments investigating wake characteristics behind the turbine and an upwind configuration for the experiments focussing on the turbine loads and performance.

Acknowledgements

We would like to thank Prof. Daniel R. Parsons and his group at the University of Hull for providing the experimental data and Prof. Richard Brown and his group at the University of Strathclyde for the blade geometry. This work was funded by the Supergen Marine Challenge Programme of the EPSRC (EP/J010359/1).

References

[1] J. N. Sørensen and W. Z. Shen, *Numerical Modelling of Wind Turbine Wakes*, Journal of Fluids Engineering 124 (2002) 393–399.

[2] R. Mikkelsen, Actuator Disc Methods Applied to Wind Turbines, Ph.D. Thesis, Technical University of Denmark, Denmark, 2003.

[3] M. J. Churchfield, Y. Li and P. J. Moriarty, *A large-eddy simulation study of wake propagation and power production in an array of tidal-current turbines*, Philosophical Transactions of the Royal Society A 371 (2015) 1–15.

[4] M. H. Baba-Ahmadi and P. Dong, *Validation of Applying Actuator Line Model to Horizontal Axis Tidal Stream Turbines by Comparison with Detailed Measurements*, submitted to Renewable Energy, RENE-D-15-01118.

[5] S. Gant and T. Stallard, *Modelling a Tidal Turbine in Unsteady Flow*, in Proceedings of the Eighteenth International Offshore and Polar Engineering Conference, Vancouver, BC, Canada, July 2008 473–480.

[6] N. Troldborg, J. N. Sørensen, R. Mikkelsen and N. N. Sørensen, A simple atmospheric boundary layer model applied to large eddy simulations of wind turbine wakes, Wind Energy 17 (2014) 657–669. DOI: 10.1002/we.1608.

[7] N. Troldborg, F. Zahle, P. E. Réthoré and N. N. Sørensen, Comparison of wind turbine wake properties in non-sheared inflow predicted by different computational fluid dynamics rotor models, Wind Energy 18 (2015) 1239–1250, DOI: 10.1002/we.1757.

[8] J. Mann, Wind field simulations, Probabilistic Engineering Mechanics 13 (1998) 269–282.

[9] L. Jordan, S. Simmons, S. McLelland, D. Parsons, L. Vybulkova, *The impact of tidal stream turbines on 3D flow and bed shear stress measured with particle image velocimetry in a laboratory flume*, In Proceedings of The 11th European Wave and Tidal Energy Conference (EWTEC) Nantes, France, Sept. 2015.

[10] M. H. Baba-Ahmadi and G. R. Tabor, *Inlet Conditions for LES using Mapping and Feedback Control*, Computers & Fluids 38 (2009) 1299–1311.

[11] M. H. Baba-Ahmadi and G. R. Tabor, *Inlet Conditions for Large Eddy Simulation of Gas-Turbine Swirl Injector*, AIAA J. 46 (7) (2008) 1782–1790.

[12] S. Menon, P. K. Yeung and W. W. Kim, *Effect of Subgrid Models on the Computed Interscale Energy Transfer in Isotropic Turbulence*, Computers & Fluids 25(2) (1996) 165–180.

[13] N. Troldborg, Actuator Line Modeling of Wind Turbine Wakes, Ph.D. Thesis, Technical University of Denmark, Denmark, 2008.

[14] W. Z. Shen, W. J. Zhu and J. N. Sørensen, *Actuator line/Navier-Stokes computations for the MEXICO rotor: comparison with detailed measurements*, Wind Energy 15(5) (2012) 811–825.

[15] H.G. Weller, G. R. Tabor, H. Jasak, C. Fureby, A tensorial approach to computational continuum mechanics using object orientated techniques, Computational Physics 12 (6) (1998) 620–631.

[16] OpenFOAM, Released via the OpenFOAM Foundation, See http://openfoam.org.

[17] C.M. Rhie and W.L. Chow, *A Numerical Study of the Turbulent Flow Past an Isolated Airfoil with Trailing Edge Separation*, AIAA. J. 21 (1983) 1225–1232.

[18] A. Chaudhari, Large eddy simulation of wind flows over complex terrains for wind energy applications, Ph.D. Thesis, Lappeenranta University of Technology, Lappeenranta, Finland 2014.

[19] C. A. Consul, R. H. J. Willden and S. C. McIntosh, Blockage effects on the hydrodynamic performance of a marine cross-flow turbine, Philosophical Transactions of the Royal Society A 371: 20120299.

[20] XFOIL, See https://stuff.mit.edu/afs/athena/software/aeroutil-v1.0/Xfoil.

[21] S. C. Tedds, I. Owen and R. J. Poole, *Near-wake Characteristics of a Model Horizontal Axis Tidal Stream Turbine*, Renewable Energy, 63, (2014) 222–235.